Cloud-Level Penetrative Compressible Convection in the Venus Atmosphere

R. DAVID BAKER AND GERALD SCHUBERT

Department of Earth and Space Sciences and Institute of Geophysics and Planetary Physics, University of California, Los Angeles, Los Angeles, California

PHILIP W. JONES

Theoretical Division, Los Alamos National Laboratory, Los Alamos, New Mexico

(Manuscript received 3 May 1996, in final form 4 April 1997)

ABSTRACT

A two-dimensional, nonlinear, fully compressible model of a perfect gas is used to simulate cloud-level penetrative convection in the Venus atmosphere from 40 to 60 km altitude. Three cases with different amounts of solar heating are considered: 60%, 80%, and 100% subsolar heating conditions corresponding to maximum internally heated Rayleigh numbers of 4.0×10^6, 5.4×10^6, and 6.8×10^6, respectively. Cloud-level convection is characterized by cold, narrow downwellings that deeply penetrate ($\sim$5 km) the underlying stable layer. The horizontal spacing of the downwellings is 15–30 km, an order of magnitude smaller than observed cloud-top cells in ultraviolet images. The penetrating head of the downflow is both mechanically forced upward and compressionally heated by the underlying stable layer. The local compressional heating rate induced by penetration is four orders of magnitude larger than the solar heating rate. Although slightly larger in magnitude, the calculated vertical velocities at 54-km altitude are consistent with *Vega* balloon measurements. The computations show that the *Vega* balloons drifted in a relatively quiescent part of the convection layer. Vertical velocities are three to five times larger in the lower part of the convection layer than in the upper part of the layer because of the dominance of convection by intense downwellings that acquire their highest speeds as they penetrate the underlying stable region. Mixing length theory underestimates the vertical velocity of convection by a factor of 3 or more because kinetic energy in the convection layer is balanced not only by buoyancy work as assumed by mixing length theory, but also by pressure work and viscous work. A transfer of energy from low-frequency convective modes to higher-frequency ''interfacial'' penetrative modes occurs in the penetrative region. Internal gravity waves are also generated in the stable layers with horizontal wavelengths of 5–30 km and intrinsic horizontal phase speeds comparable to convective velocities.

1. Introduction

Cellular convection has long been thought to occur in the clouds of Venus (Belton et al. 1976, 1991; Rossow et al. 1980; Covey and Schubert 1981; Baker and Schubert 1992). Ultraviolet images of the cloud tops $\sim$60–70 km above the surface from the *Mariner 10, Pioneer Venus,* and *Galileo* spacecraft show polygonal features in the subsolar region with horizontal scales of roughly 200–1000 km. Both dark-rimmed and bright-rimmed cells are observed, with the dark-rimmed cells slightly larger and more common. These cells are predominantly found in the afternoon and in low latitudes (Murray et al. 1974; Rossow et al. 1980; Belton et al. 1991; Baker and Schubert 1992; Toigo et al. 1994) with a lifetime of roughly 2 days (Toigo et al. 1994).

Further evidence for convection in the Venus atmosphere is obtained from radio occultation and spacecraft probe data. Radio occultation experiments with the *Mariner 10* (Howard et al. 1974) and *Magellan* (Jenkins et al. 1994) spacecraft indicate neutrally stable regions from 47 to 55 km altitude and 50 to 55 km altitude, respectively. Temperature and pressure measurements from *Pioneer Venus* probes show two neutrally stable regions, one in the lower atmosphere from roughly 18 to 30 km above the surface and a cloud-level adiabatic layer in the altitude range 48–55 km (Seiff et al. 1980). This thermal structure was later confirmed by the *Vega* lander probe (Young et al. 1987). These layers are likely sites of convection since convective overturning forces the thermal structure toward adiabaticity. In addition, *Vega* balloons measured vertical velocities within the cloud-level adiabatic layer of 1–3 m s^{-1} (Linkin et al. 1986). These velocities are well correlated with thermal perturbations in the region, indicating that convection is occurring in the cloud layer (Ingersoll et al. 1987).

The large size of the cellular features in the subsolar region has yet to be adequately explained. If these

Corresponding author address: Dr. R. David Baker, Dept. of Earth and Space Sciences, UCLA, Box 951567, 3806 Geology Bldg., Los Angeles, CA 90095-1567.
E-mail: rbaker@artemis.ess.ucla.edu

features originate in the cloud-level adiabatic region, as commonly assumed, the aspect ratio (width/height) of the cells is of order 10^2, an order of magnitude larger than observed for mesoscale cellular convection on Earth (Agee 1987) and two orders of magnitude larger than for laboratory experiments (Tritton 1975). A number of mechanisms have been hypothesized to explain the large aspect ratios on Venus. Tritton (1975) observed that laboratory experiments with internal heat generation produce larger aspect ratio cells than bottom-heated experiments and suggested that solar absorption in the clouds of Venus could similarly produce wider cells. However, internally heated laboratory experiments produce cells with aspect ratio of at most 5, much smaller than aspect ratios observed in the Venus atmosphere. Anisotropic eddy diffusion has also been proposed as a mechanism for producing long wavelength cells on Venus. Linear stability analysis for the Venus atmosphere indicates that the degree of anisotropy must be roughly 100 in order to produce the required aspect ratios (Covey and Schubert 1981). Deep penetrative convection may also explain the large cells observed on Venus. Convection in the clouds may penetrate the underlying stable region, interact with upward penetration from the lower convection layer through wave–convection coupling, and effectively form whole-atmosphere convection from the surface to the cloud tops with the convective layer depth larger by an order of magnitude. The aspect ratios of the cells would then more closely resemble those on Earth (Baker and Schubert 1992).

Cloud-level penetrative convection likely generates small-scale gravity waves in the Venus atmosphere (Schubert 1983; Schubert and Walterscheid 1984; Schinder et al. 1990; Baker and Schubert 1992; Seiff et al. 1992; Leroy 1994; Leroy and Ingersoll 1995, 1996). Bowlike features and wave trains are abundant in cloud-top ultraviolet images (Belton et al. 1976; Rossow et al. 1980). Doppler tracking of the *Pioneer Venus* north probe (Seiff et al. 1980) and *Magellan* radio occultation experiments (Jenkins et al. 1994; Hinson and Jenkins 1995) detected gravity wave oscillations below the convection layer. The proximity of these waves to the convection region suggests that penetrative convection may be a principal wave generating mechanism in the Venus atmosphere.

Up to this point, treatments of cloud-level convection in the Venus atmosphere have been subject to numerous simplifications. One-dimensional radiative–convective models (Pollack et al. 1980) parameterize convection through convective adjustment in which the temperature profile is set to the adiabat when the radiative profile is superadiabatic. Heat transfer by convection and the effects of penetration are neglected by this treatment. Mixing length theory has been used to estimate the overturning time of cloud-level convection (Toigo et al. 1994) and to prescribe convective velocities for gravity wave generation (Leroy 1994; Leroy and Ingersoll 1995, 1996). Mixing length theory assumes the Boussinesq approximation, which requires the depth of the convection layer to be much smaller than a scale height (Spiegel and Veronis 1960). In the Venus clouds, the depth of the neutrally stable layer ($\sim$7 km) is comparable to the pressure scale height at 51.5-km altitude ($\sim$7.2 km), thus invalidating mixing length treatments of cloud-level convection. As our simulations show, convection in the clouds of Venus can, in fact, span nearly two scale heights.

The purpose of this paper is to explore the nature of convection in the cloud region of the Venus atmosphere. A nonlinear, fully compressible numerical model is used to study penetrative convection from 40 to 60 km altitude. Venus-like profiles of temperature, density, and solar heating are used. Three cases with different amounts of solar energy absorption are considered: 60%, 80%, and 100% of the solar absorption at the subsolar point. We begin by presenting our mathematical model of the Venus atmosphere and the numerical approach. Section 3 describes the results of our numerical simulations, and the last section discusses the implications of these results for the atmosphere of Venus.

2. Model

a. Model equations and numerical method

We consider two-dimensional, nonlinear, fully compressible motions in a plane-parallel atmosphere. Compressibility is important on two counts: 1) convective motions may span multiple scale heights in these simulations, thereby rendering the standard Boussinesq approximation inappropriate to study cloud-level convection in the Venus atmosphere, and 2) compression enhances the negative buoyancy of downwellings, making downflow plumes narrower than those found in Boussinesq or anelastic systems (Hurlburt et al. 1984). We assume a Venus-like background state supported by unmodeled processes such as thermal radiation or large-scale dynamics and consider time-dependent convective motions superimposed on this background state. Absorption of solar radiation drives convection in the cloud layer. We scale the nonlinear, fully compressible equations by the layer depth d, reference density ρ_0, reference temperature T_0, reference volumetric heating q_0, and reference sound crossing time $d/(RT_0)^{1/2}$, where R is the gas constant and the reference level is at 60-km altitude. The resulting nondimensional equations are

$$\frac{\partial \rho'}{\partial t} = -\frac{\partial}{\partial x_i}(\rho u_i') \tag{1}$$

$$\frac{\partial}{\partial t}(\rho u_i') = -\frac{\partial}{\partial x_j}(\rho u_i' u_j' + p'\delta_{ij} - \sigma C_k \tau_{ij}') - C_g \rho' \delta_{i3} \tag{2}$$

$$\frac{\partial \theta'}{\partial t} = -\frac{\partial}{\partial x_i}[(\bar{\theta} + \theta')u_i'] + (\bar{\theta} + \theta')\frac{\partial u_i'}{\partial x_i} + \frac{C_k}{\rho}\frac{\partial}{\partial x_i}\left(\rho\kappa\frac{\partial \theta'}{\partial x_i}\right) + \frac{\gamma - 1}{\gamma}\frac{\sigma C_k}{\rho}\tau_{ij}'\frac{\partial u_j'}{\partial x_i} + \frac{C_q}{\rho}Q', \tag{3}$$

where u_i is velocity in the x_i direction, p is pressure, ρ is density, θ is potential temperature, t is time, κ is eddy diffusivity, Q is volumetric internal heating by solar energy absorption, and τ_{ij} is the eddy stress tensor given by

$$\tau_{ij}' = \rho\kappa\left(\frac{\partial u_i'}{\partial x_j} + \frac{\partial u_j'}{\partial x_i}\right), \tag{4}$$

and σ, γ, C_g, C_k, and C_q are parameters defined below. All quantities are nondimensional. Total variables (e.g., θ) are decomposed into background state variables $\bar{\theta}$ and deviations from this background state θ'. Eddy diffusion acts only on deviation quantities; that is, the background state is unaffected by turbulent eddies. The conservation equations are augmented by an equation of state, which is given by the nondimensional perfect gas law

$$p = (\rho\theta)^{\gamma}. \tag{5}$$

The fully compressible system is characterized by five nondimensional parameters:

$$\sigma = \frac{\kappa_m}{\kappa_\theta} \tag{6}$$

$$\gamma = \frac{c_p}{c_v} \tag{7}$$

$$C_g = \frac{dg}{RT_0} \tag{8}$$

$$C_k = \frac{\kappa_\theta}{d(RT_0)^{1/2}} \tag{9}$$

$$C_q = \frac{dq_0}{\rho_0 c_p T_0 (RT_0)^{1/2}}. \tag{10}$$

In (6)–(10), all quantities on the right-hand sides are dimensional, κ_m is the reference eddy momentum diffusivity, κ_θ is the reference eddy thermal diffusivity, c_p is the specific heat at constant pressure, c_v is the specific heat at constant volume, and g is the acceleration of gravity. The Prandtl number σ represents the relative strength of momentum diffusion compared with heat diffusion, and γ determines the density change during adiabatic pressure fluctuations. The parameter C_g may be interpreted as the ratio of the time for a sound wave to travel a distance d (the sound crossing time) to the free fall time through a layer with depth d, or alternatively, as the ratio of the depth of the layer to the isothermal scale height at the reference level. The quantity C_k is the ratio of the sound crossing time to the thermal diffusion time, and C_q is the ratio of the sound crossing time to the characteristic heating time.

Classic Boussinesq treatments of internally heated convection are characterized by two nondimensional parameters, the Prandtl number σ and the internally heated Rayleigh number Ra_q. The Rayleigh number represents the relative efficiency of buoyancy forces due to internal heat generation in overcoming diffusion and can be expressed in terms of the nondimensional compressible parameters

$$\mathrm{Ra}_q = \frac{g q_0 d^5}{T_0 \rho_0 c_p \kappa_\theta^2 \kappa_m} = \frac{C_g C_q}{\sigma C_k^3}. \tag{11}$$

In steady state, the horizontal average of the total energy equation may be expressed nondimensionally as

$$\frac{d}{dz}(F_c + F_e + F_k + F_p + F_v + F_q) - (W_b - W_p) = 0, \tag{12}$$

where F_c is the convective heat flux, F_e is the eddy diffusive heat flux, F_k is the kinetic energy flux, F_p is the energy flux associated with pressure fluctuations, F_v is the viscous flux, F_q is the solar energy flux, W_b is the rate of work by buoyancy, and W_p is rate of pressure work associated with volume changes. Equation (12) asserts that, in steady state, the horizontally averaged work by buoyancy and pressure is balanced by the divergence of energy fluxes at that altitude. The nondimensional flux and work terms are defined as

$$F_c = \langle \rho\theta'' w' \rangle \tag{13}$$

$$F_e = -C_k\left\langle \rho\kappa\frac{d\theta'}{dz}\right\rangle \tag{14}$$

$$F_k = \frac{1}{2}\frac{(\gamma - 1)}{\gamma}\langle \rho u_i' u_i' w' \rangle \tag{15}$$

$$F_p = \frac{(\gamma - 1)}{\gamma}\langle p'' w' \rangle \tag{16}$$

$$F_v = -\frac{(\gamma - 1)}{\gamma}\sigma C_k \langle u_i' \tau_{iz}' \rangle \tag{17}$$

$$F_q = C_q \langle F_Q' \rangle \tag{18}$$

$$W_b = -\frac{(\gamma - 1)}{\gamma} C_g \langle \rho'' w' \rangle \tag{19}$$

$$W_p = -\frac{(\gamma - 1)}{\gamma}\left\langle p'' \frac{\partial u_j'}{\partial x_j} \right\rangle, \tag{20}$$

where the angle brackets indicate a horizontal average, a double prime indicates residuals from the horizontal average, z denotes the vertical coordinate, w is the vertical velocity, and F_Q' represents the vertical integral of volumetric solar heating Q'. We use the convention that upward energy or heat transfer is positive. Similarly, the horizontal average of the steady-state mechanical energy equation can be expressed nondimensionally as

$$\frac{d}{dz}(F_k + F_p) - (W_b + W_p - W_v) = 0, \tag{21}$$

where W_v is the rate of work by viscous stresses

$$W_v = \frac{(\gamma - 1)}{\gamma}\sigma C_k \left\langle u_i' \frac{\partial \tau_{ij}'}{\partial x_j} \right\rangle. \tag{22}$$

Equations (1)–(3) are solved explicitly in time using a second-order time-adaptive leapfrog scheme for all but the diffusion terms, which are solved using an implicit Crank–Nicolson scheme in the energy equation and an explicit time-lag scheme in the momentum equations to avoid computational instability. Spatial derivatives are computed using centered, second-order differences on a vertically staggered grid. A frequency filter (Asselin 1972) with a filter factor of 0.02 is applied at every time step to dampen the leapfrog computational mode. The code has been benchmarked successfully against a bottom-heated Boussinesq study (Moore and Weiss 1973), an internally heated Boussinesq study (Thirby 1970), and two bottom-heated, fully compressible cases (Graham 1975).

b. Input parameters for the Venus atmosphere

A steady, Venus-like background state is implemented to account for physical processes not directly included in our model, such as longwave thermal radiation and large-scale dynamics, that influence the vertical structure of the Venus atmosphere on timescales much longer than the convective timescale. The vertical profile of static stability of the background state is shown in Fig. 1. This profile is consistent with those measured by the *Pioneer Venus* probes (Seiff et al. 1980) and the *Vega-2* lander (Young et al. 1987). Convection in the cloud layer inhibits the influence of thermal radiation from 48 to 55 km altitude by transporting excess heat out of the region before thermal radiation can affect the vertical structure. The background state incorporates this long-term effect by including an adiabatic region from 48 to 55 km altitude. For this study, the mean zonal wind of the background state is assumed to be zero in order to ascertain the nature of penetrative convection in the absence of shear. Future investigations will include a Venus-like wind profile to determine the effects of shear on penetrative convection.

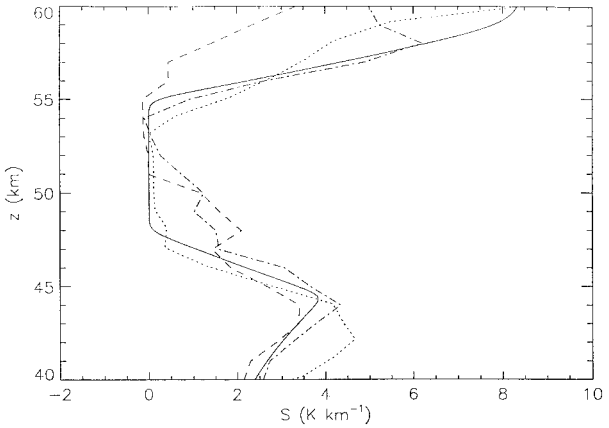

FIG. 1. Static stability profile for the Venus background state (solid line). The dashed line is from the *Pioneer Venus* North probe and the dash-dot line is from the *Pioneer Venus* Sounder (Seiff et al. 1980). The dotted line is from the *Vega-2* lander (Young et al. 1987).

Flux measurements from the *Pioneer Venus* probes indicate that solar radiation is predominantly absorbed in the clouds (Tomasko et al. 1980). It is this absorption of solar energy that drives convection in the cloud region. Using the globally averaged net solar flux calculated from *Pioneer Venus* measurements and the relationship describing solar flux variation with cosine of the zenith angle μ_0 (Tomasko 1983),

$$F_s(\mu_0, z) = F_{\text{sub}}(z)\mu_0^{1.4}, \tag{23}$$

the solar flux at the subsolar point $F_{\text{sub}}(z)$ can be determined. Differentiation of $F_{\text{sub}}(z)$ with respect to z gives the volumetric subsolar heating $Q_{\text{sub}}(z)$. A pair of Gaussian distributions provides an excellent fit to the heating data,

$$Q_{\text{sub}}(z) = c_L \exp\left(\frac{-(z - z_L)^2}{2\sigma_L^2}\right) + c_U \exp\left(\frac{-(z - z_U)^2}{2\sigma_U^2}\right), \tag{24}$$

where $c_L = 3.6 \times 10^{-3}$ W m^{-3}, $z_L = 27$ km, $\sigma_L = 13$ km, $c_U = 2.7 \times 10^{-2}$ W m^{-3}, $z_U = 67$ km, $\sigma_U = 7.5$ km, and z is in kilometers. This relationship holds from 0 to 100 km altitude (Fig. 2) and agrees quite well with solar heating estimates of Tomasko et al. (1985) and the Venus solar model used by Hou and Goody (1989). For the vertical extent considered in this study (altitude 40–60 km), most of the solar heating occurs near the top of the domain.

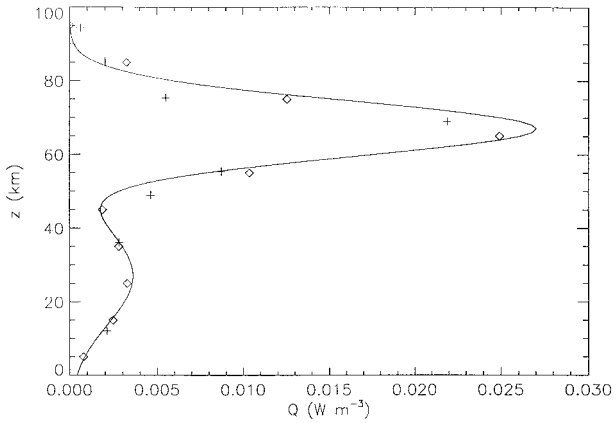

FIG. 2. Model solar heating at the subsolar point from (24). The plus signs are estimated heating rates based on *Pioneer Venus* data (Tomasko et al. 1985). The diamonds are from the Venus solar heating model of Hou and Goody (1989).

TABLE 1. Venus model parameter values.

Parameter	Value	Nondimensional Parameter	Value
g	8.87 m s^{-2}		
R	191.4 J kg^{-1}K^{-1}		
c_p	891 J kg^{-1}K^{-1}	σ	1.00
κ_m	155 m^{2}s^{-1}	γ	1.27
κ_θ	155 m^{2}s^{-1}	C_g	3.46
d	20.0 km	C_k	3.42×10^{-5}
ρ_0	0.4291 kg m^{-3}	C_q	9.12×10^{-6}
T_0	268 K		1.21×10^{-5}
q_0	1.06×10^{-2} W m^{-3}		1.52×10^{-5}
	1.40×10^{-2} W m^{-3}		
	1.76×10^{-2} W m^{-3}		

Absorbed solar radiation at the subsolar point also drives large-scale dynamics and infrared radiative transfer. The partitioning of solar heating into small-scale and large-scale dynamical forcing is difficult to estimate since convection and large-scale dynamics often interact. Convection in the subsolar region of Venus may strongly influence and even help organize large-scale motions, similar to cumulus–synoptic scale interaction in Earth's Tropics (Holton 1979). Both convection cell lifetimes (Toigo et al. 1994) and the turbulent eddy diffusion timescale are roughly 2 days in length, yet the radiative timescale from 40 to 60 km altitude is 200–1300 days (Pollack and Young 1975). Because dynamical timescales are much shorter than radiative timescales at these altitudes, we believe that most of the solar radiation absorbed in this altitude interval is balanced by dynamics. We consider three different solar heating cases to drive convective motions: 60%, 80%, and 100% subsolar heating. These three cases offer a range of possible convective states in the subsolar region. The 100% subsolar heating case is the upper limit for driving convection by solar energy absorption.

Table 1 gives values of input parameters and the resulting nondimensional parameters for the Venus model atmosphere. The quantities g, R, c_p, κ_m, and κ_θ are assumed uniform with height. The value of c_p used in this model is appropriate for a temperature of 350 K (Staley 1970), the mean temperature at 50-km altitude. The values of the eddy diffusion coefficients κ_m and κ_θ are consistent with recent estimates of 120–150 m^{2}s^{-1} from radio scintillation data on scales less than 1 km (Leroy 1994). Photochemical modeling suggests diffusion coefficients two orders of magnitude smaller (Krasnopolsky and Parshev 1981, 1983; Krasnopolsky 1985; Yung and DeMore 1982). This value of eddy diffusion may not be appropriate for modeling small-scale turbulence since eddy diffusion in photochemical models also parameterizes large-scale dynamics, including convective motions explicitly resolved in our model. A Prandtl number of unity is used since turbulence equally diffuses momentum and heat.

The Rayleigh number defined by (11) uses the total depth d of the layer. Although the effects of convective penetration do span the entire depth d, we choose a more conservative value of the convective depth to define the effective Rayleigh number Ra_q^* (similar to Ra_q but based on a depth smaller than d). The neutrally stable region of the background state occurs from 48 to 55 km. Using this depth of 7 km and the values of solar heating at 55 km (the maximum value in the neutrally stable region), the effective Rayleigh numbers Ra_q^* corresponding to the three cases are 4.0×10^6, 5.4×10^6, and 6.8×10^6. Rayleigh numbers Ra_q based on the total depth d are of order 10^9.

The computational domain spans the altitude range 40–60 km and extends 180 km horizontally. The vertical resolution is 168 grid points and the horizontal resolution is 1000 grid points. A large number of horizontal grid points is required to resolve the extremely narrow downflow plumes in these simulations. Consequently, the horizontal domain is too small to address the development of cells with horizontal scales of 1000 km but is sufficiently large to address the tendency of long wavelength cell growth on the order of 100 km.

The horizontal boundaries are stress free with a fixed heat flux, and the side boundaries are periodic. Fixed flux boundary conditions are appropriate for Venus because the values of eddy diffusion below 40-km altitude and above 60-km altitude probably do not differ greatly from the value within the layer. In order for fixed temperature boundary conditions to apply, the diffusion coefficient outside the layer would need to be much larger than the value inside the layer so that heat could be removed quickly enough to maintain a constant temperature at the boundary (Sparrow et al. 1964). Although thermal radiation to space would act to maintain a constant temperature at 60-km altitude, the radiative time constant at 60-km altitude (Pollack and Young 1975) is an order of magnitude larger than the eddy diffusion timescale. Fixed flux boundary conditions are therefore appropriate for cloud-level convection in the

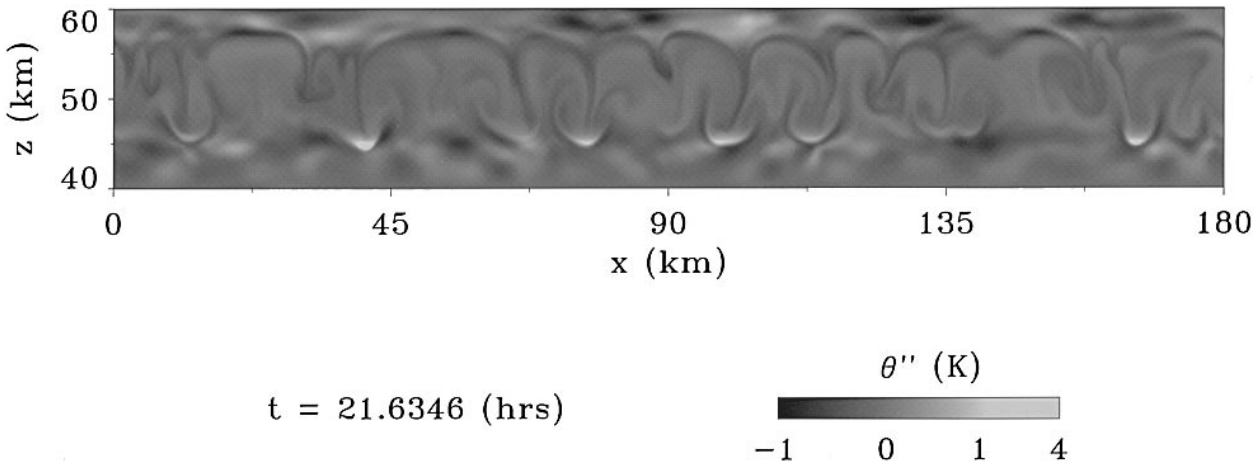

FIG. 3. Residual potential temperature for the 100% subsolar heating case. The underlying stable layer runs from 40 to 47 km, the convection layer from 47 to 56 km, and the overlying stable layer from 56 to 60 km. The penetrative region exists from 43 to 47 km.

Venus atmosphere. The value of heat flux at the boundaries is equal to but opposite in sign from the solar flux at that level. The impermeable, stress-free boundary condition causes artificial wave reflection at the upper and lower boundaries. An additional 100% subsolar heating case with sponge layers at the top and bottom to absorb vertically propagating waves has been performed to test the effect of reflecting gravity waves on convective planform. Sponge layers are implemented using Rayleigh damping terms whose coefficients have an exponential dependence on altitude. The vertical extent for the sponge layer case is 35–65 km with strong damping below 40 km and above 60 km.

The 80% case was started from a lower Rayleigh number solution (higher eddy diffusion coefficient) and the 60% and 100% cases began from the final 80% solution. Since our model includes sound waves, a small time step of approximately 0.125 s is required to meet the Courant condition for stability. The 60% and 100% cases were integrated for 15.6 and 25.0 simulation hours, respectively. This length of time was sufficient to pass the transient phase and establish a stable, time-dependent flow. The 80% case was integrated for a longer period of time (32.8 simulation hours) to ensure that a dramatic planform change did not occur within a significant portion of the observed Venus cell lifetime of ~50 h (Toigo et al. 1994).

3. Results

a. General characteristics of cloud-level convection

Figure 3 shows residual potential temperature θ'' (total potential temperature minus horizontally averaged potential temperature) for the 100% subsolar heating case. This figure illustrates features representative of cloud-level penetrative compressible convection for the three heating cases considered. Differences among the three heating cases will be discussed as needed. The convection is dominated by cold, narrow downwellings, characteristic of both internally heated (Peckover and Hutchinson 1974) and compressible convection (Hurlburt et al. 1984). The downflow plumes have horizontal widths of 1–2 km, while the horizontal scale of the cells is 15–30 km. The downflow plumes penetrate the underlying stable layer and are both mechanically forced upward and compressionally heated by the stable layer. The local volumetric heating of the compression regions found at 45-km altitude is roughly 20 W m^{-3}, four orders of magnitude larger than the heating due to absorption of solar energy. The strong downward penetration generates internal gravity waves in the underlying stable layer. Spectral analysis of θ'' at 42-km altitude (not shown) indicates horizontal wavelengths of 5–30 km.

The flow is highly time dependent, with adjacent starting downwellings merging together to create single, strong downward plumes. The locations of these strong plumes are relatively stable, although gravity wave feedback can cause the plumes to sway horizontally by as much as 5 km. The time dependence can be seen in the time series plot of kinetic energy density for the three cases (Fig. 4). The kinetic energy density represents the average kinetic energy of the entire domain. Spectral analysis of the kinetic energy density time series indicates that the 60%, 80%, and 100% subsolar heating cases have dominant periods of 115 min, 117 min, and 126 min, respectively. We attribute these periods to the convective overturn time of the system. The longer overturn time with increased solar heating is caused by an increase in the convection layer depth. Shorter period oscillations of ~45 min are associated with the penetrative cycle. Both convection layer depth and penetrative cycle are discussed in more detail below. Naturally, higher solar heating (higher Ra_q) calculations exhibit larger time-average values of kinetic energy density. The time-average kinetic energy density of the 100% subsolar case (8.16 J m^{-3}) is comparable to the kinetic

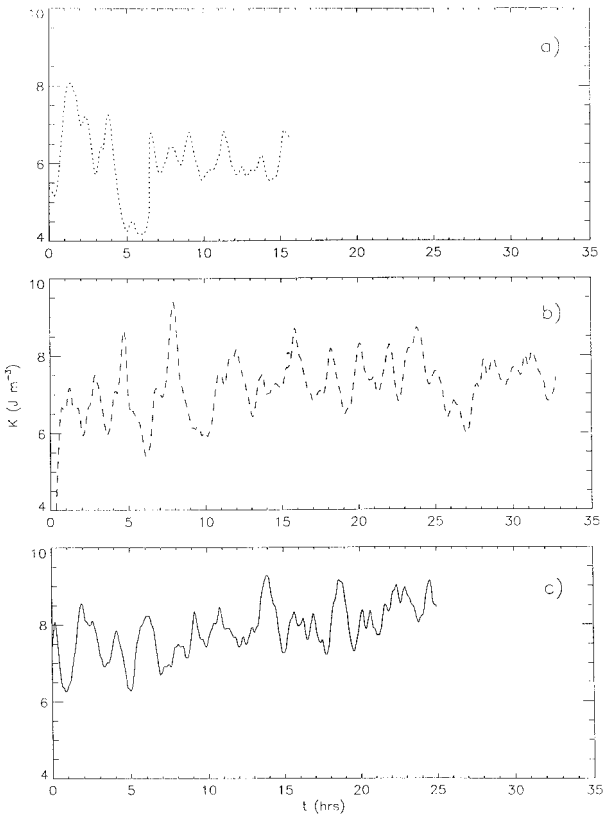

FIG. 4. Time series of kinetic energy density (mean kinetic energy in the entire domain) for (a) 60% subsolar heating, (b) 80% subsolar heating, and (c) 100% subsolar heating.

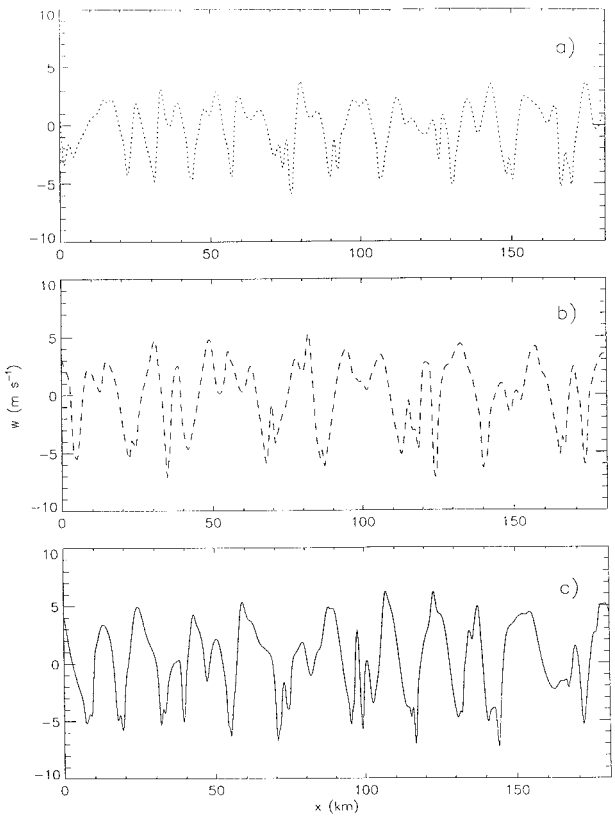

FIG. 5. Vertical velocity at 54-km altitude as a function of horizontal position for (a) 60% subsolar heating, $t = 15.0$ h, (b) 80% subsolar heating, $t = 24.1$ h, and (c) 100% subsolar heating, $t = 13.8$ h. The velocities were sampled at times corresponding to peaks in the kinetic energy density.

energy of a convective shower on Earth (Emanuel 1994). However, in regions near strong convective downdrafts, the mean value of kinetic energy density for the 100% subsolar case (38.5 J m^{-3}) is more comparable to intense supercell thunderstorms on Earth (Brandes 1978).

Figure 5 shows the vertical velocity at 54-km altitude as a function of horizontal position at times corresponding to peaks in the kinetic energy density for the three cases considered. This altitude corresponds to the average altitude of the *Vega* balloons, which measured vertical velocities of roughly 1–3 m s^{-1} (Linkin et al. 1986). Because the velocities in Fig. 5 were sampled at peaks in the kinetic energy plots of Fig. 4, the velocities favor large values; velocities during a trough in kinetic energy density versus time are lower in magnitude by roughly 1 m s^{-1}. As the amount of solar heating increases, the magnitude of the vertical velocity increases. Typical velocities for the three cases are 2–5, 4–6, and 5–7 m s^{-1}, respectively, with maximum (downward) velocities of -5.9, -7.1, and -7.3 m s^{-1}. These velocities are consistent with *Vega* balloon measurements because the balloons sampled velocities in the early morning (roughly 0000–0800 local Venus time) and our simulations occur near the subsolar point where velocities should be larger. At an altitude of 54 km, the width of downward motion is comparable to the width of upward flow and the magnitude of the vertical velocity is relatively small because we are near the top of the convection region where downwellings originate. Higher downward velocities are found just above the underlying stable layer where downwellings are more concentrated (maximum velocities of -11.1, -13.6, and -14.2 m s^{-1}, respectively).

The solar energy flux F_q through the adiabatic layer from 48 to 55 km is primarily balanced by convective heat transfer F_c as seen in Fig. 6 for the 100% subsolar heating case. Values of F_c are larger at a kinetic energy peak (Fig. 6a) than at a kinetic energy trough (Fig. 6b). The regions of negative F_c indicate regions of convective penetration or entrainment. Convective penetration occurs in the underlying stable layer when the downwelling ($w' < 0$) forces relatively warm air ($\theta'' > 0$) downward. Convective entrainment occurs in the overlying stable layer when warmer stable air is pulled downward by convection underneath. At times of peak kinetic energy density, intense penetration into the underlying stable layer occurs, as shown by the strong negative values of F_c around 45-km altitude (Fig. 6a). This penetration is less intense at a kinetic energy trough

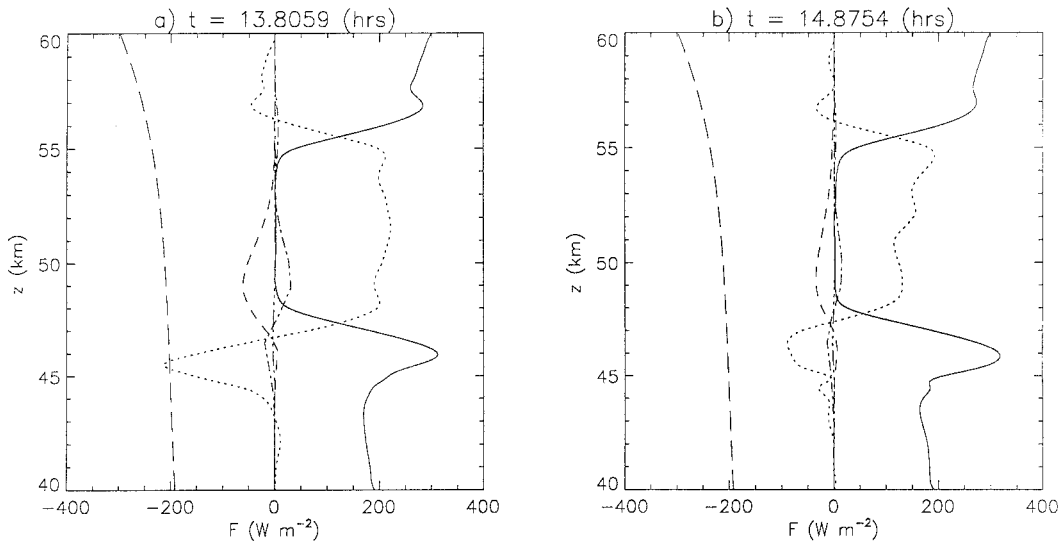

FIG. 6. Energy fluxes through the layer for the 100% subsolar heating case at (a) a kinetic energy peak and (b) a kinetic energy trough. Plotted are the convective energy flux F_c (dot), the eddy diffusive flux F_e (solid), the kinetic energy flux F_k (short dash), pressure work F_p (dash-dot), viscous flux F_v (dash-triple dot), and the solar flux F_q (long dash), all scaled by the solar flux at the top. Positive values indicate upward energy or heat transfer.

(Fig. 6b). However, entrainment of the overlying stable layer is only slightly stronger during peak kinetic energy times since most of the kinetic energy resides at lower altitudes where both density and velocities are larger. The kinetic energy flux F_k is negative in the convection layer because the flow is dominated by cold, narrow downwellings. This characteristic has also been observed in simulations of compressible solar convection (Hurlburt et al. 1984, 1986; Jones 1991). Compressional heating in the underlying stable layer is indicated by negative values of pressure flux F_p around 46-km altitude. The relatively small value of F_p occurs because the compressional features, although they generate heat four orders of magnitude larger than solar heating, are local features separated by large expanses where no compressional heating occurs (Fig. 3).

b. Comparison with mixing length theory

Mixing length theory is a simple approach used to quantify the physical processes that occur in a convection layer. For a complete development of mixing length theory, we refer the reader to Cox and Giuli (1968) and Hansen and Kawaler (1994). Briefly, a parcel of air moves vertically and retains its density and temperature through a mixing length *l.* Upon traveling a mixing length *l,* the parcel mixes with the environment and deposits its energy at the new altitude. Several simplifying assumptions are used in developing mixing length theory: the mixing length *l* is much shorter than a scale height, the velocity of the parcel is sufficiently slow to allow the parcel pressure to adjust to the environmental pressure as the parcel rises or descends, acoustic phenomena are negligible, and the density and temperature of the parcel differ a small amount from the environmental values. These requirements comprise the Boussinesq approximation (Spiegel and Veronis 1960). In addition, the kinetic energy of the parcel is assumed to balance the buoyancy work done on the parcel. Under these assumptions, mixing length theory associates the convective heat flux with the vertical velocity or superadiabatic gradient within the layer. It is commonly used to determine the amount of heat transported by convection in stellar envelopes (Hansen and Kawaler 1994). Mixing length theory has been applied to the Venus atmosphere to compare convective velocities with *Vega* balloon measurements (Blamont et al. 1986), to estimate the convective overturn times in both the cloud-level convection layer and the convection layer near the surface (Toigo et al. 1994), and to generate internal gravity waves by cloud-level convection (Leroy 1994; Leroy and Ingersoll 1995, 1996).

The vertical velocity estimated from mixing length theory is given by

$$w \approx \left(\frac{F_s g l}{\rho c_p T}\right)^{1/3}. \tag{25}$$

For a mixing length l of 7 km and evaluation of thermodynamic quantities in the middle of the convection layer at 51.5-km altitude (subsolar heat flux $F_s = 216$ W m^{-2}, $\rho = 1.29$ kg m^{-3}, and $T = 335$ K), the estimated vertical velocities for the 60%, 80%, and 100% subsolar heating cases are 2.76, 3.03, and 3.27 m s^{-1}, respectively. Although the *Vega* balloons only measured vertical velocities in the early morning, the velocity estimates from mixing length theory for the three cases considered in this paper agree with the *Vega* measured

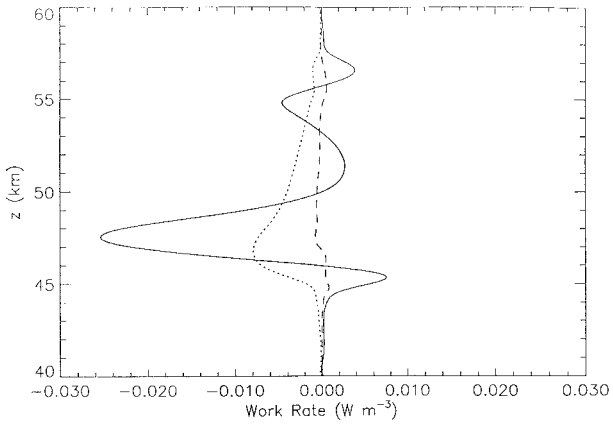

FIG. 7. Time-averaged and horizontally averaged mechanical rates of working for the 100% subsolar heating case. The solid line includes the kinetic energy and buoyancy terms of (21); the dotted line includes the kinetic energy, buoyancy, and pressure terms; and the dashed line includes the kinetic energy, buoyancy, pressure, and viscous terms.

values of 1–3 m s^{-1} (Linkin et al. 1986). However, this agreement is fortuitous. As we discuss below, mixing length theory underestimates typical convective velocities and the *Vega* balloons drifted in the relatively quiescent upper part of the convective layer.

Our numerical simulations show that mixing length theory underestimates convective velocities in the Venus cloud region. The vertical velocities in the 100% subsolar heating case range from 4 to 14 m s^{-1} with typical velocities of roughly 10 m s^{-1}, about three times larger than predicted by mixing length theory. The underestimation of the vertical velocity by mixing length theory can be attributed to a violation of the Boussinesq approximation and the assumption that kinetic energy is balanced by buoyancy work. The depth of the cloud-level convection layer is 7 km (or even deeper if penetrative effects are included). By comparison, the pressure scale height in the middle of the layer is 7.2 km. Thus, one of the major requirements of the Boussinesq approximation (depth much less than a scale height) is violated. Furthermore, the kinetic energy is balanced not only by buoyancy work but also by pressure work and viscous dissipation. Figure 7 plots the time-averaged and horizontally averaged mechanical energy work rates for the 100% subsolar heating case. The solid line represents the kinetic energy and buoyancy terms of (21). For mixing length theory to hold, this line should be close to zero everywhere. Near the top of the convection layer around 54-km altitude, this balance is marginal, but deeper in the layer where larger velocities occur, a strong imbalance exists. When the pressure terms of (21) are included, the energy balance moves closer to zero, but an imbalance remains deep in the convection layer. Viscous work completes the balance near the penetrative region since the underlying stable layer impedes convective motion and generates strong shear in the region. Further discussion of the convective velocities and the *Vega* balloon measurements will be presented in the concluding section.

c. Convective penetration

Figure 8 shows five consecutive closeup images of residual potential temperature for the 100% subsolar heating case; each frame is approximately 12.4 minutes apart. The narrow downwelling centered at about $x = 36$ km at $t = 21.4$ h has just penetrated the underlying stable layer at $z = 47$ km (Fig. 8a). Approximately 12 min later, the penetration has deepened to $z = 44$ km (Fig. 8b). A portion of the downflow plume head has been mechanically squeezed upward by the stable layer (note the cold pocket of air at $x = 41$ km, $z = 46$ km), while the remaining part of the downflow plume head is compressionally heated by the stable layer around 45-km altitude. This rapidly formed compression region is roughly 4 K warmer in potential temperature than its environment. Twelve minutes later, penetration has reached approximately 43-km altitude (Fig. 8c). Cold downflow plume air continues to be forced upward by the stable layer. The compression region has expanded and cooled. The penetrating downflow plume has generated internal gravity waves in the underlying stable layer. A new strong downwelling forms at the top of the convection layer by the convergence of smaller downwellings at $x = 35$ km. This new downwelling reaches the stable layer in 12 min (Fig. 8d) and later generates an intensely heated compressional region (Fig. 8e). The penetrative cycle in this example takes approximately 40 min.

Convective penetration and entrainment deepen the adiabatic layer in the cloud region (Fig. 9). As the amount of solar heating increases, the horizontally averaged thickness of the neutrally stable layer increases due to increased vigor of convection. The neutrally stable layer in the 100% subsolar heating case is roughly 3-km thicker than that of the background state. Solar heating destabilizes the background state stability structure in the stable layers by as much as 5 K km^{-1} at the top of the computational domain where heating is strongest. The amount of destabilization increases with increased solar heating. If the value of eddy diffusion were decreased, the stable layer would become even more destabilized since less heat would be transported out of the layer by small-scale eddies. This destabilization promotes convective penetration and entrainment by providing less resistance to vertical motion. The deepening of the adiabatic region is thus a combination of destabilization by solar heating and erosion of the stable layers by convective motions.

The horizontally averaged downward penetration depth extends to lower altitudes as the amount of solar heating increases. Using negative values of convective heat flux F_c as a diagnostic for penetration depth, we find that the horizontally averaged penetration extends down to altitudes of 43.2 km, 43.1 km, and 42.7 km

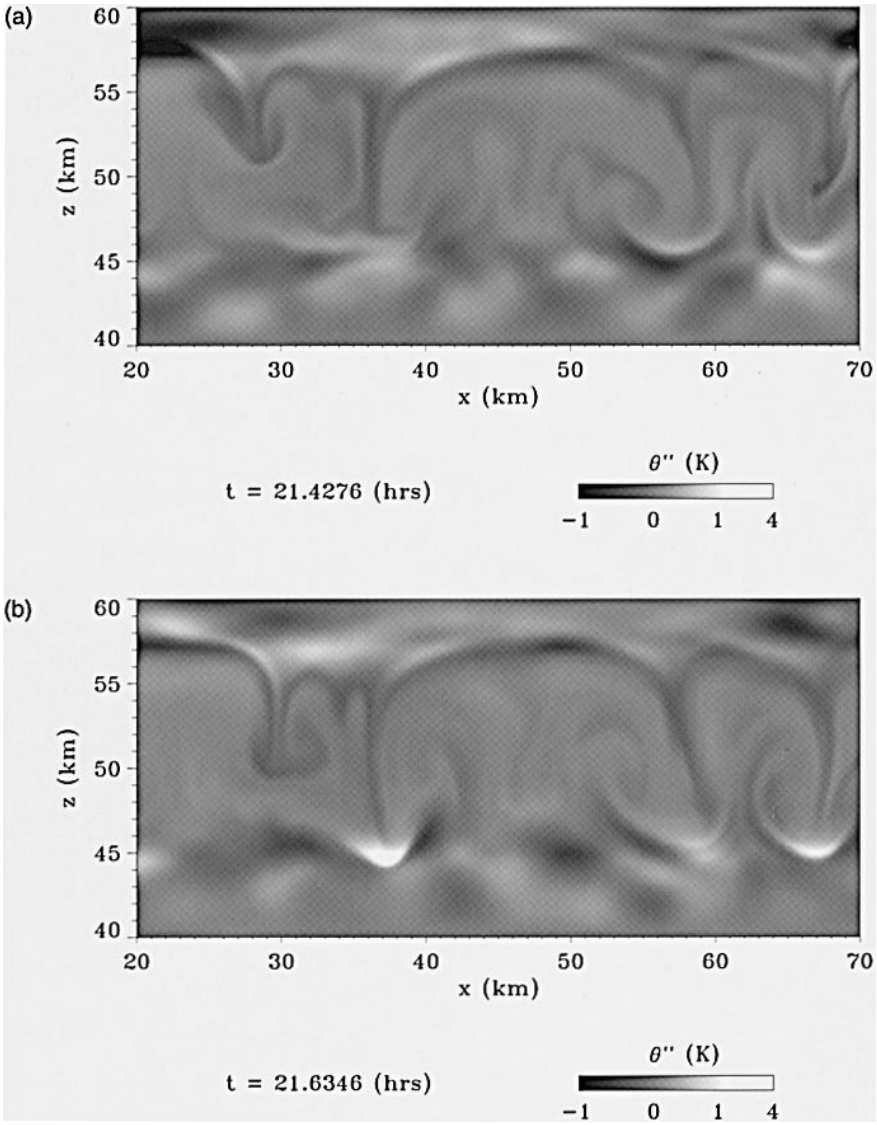

FIG. 8. Residual potential temperature for the 100% subsolar heating case of the region from $x = 20$ km to $x = 70$ km. The images are 12.4 minutes apart.

for the 60%, 80%, and 100% cases, respectively. The penetration depth oscillates with a period of ~16 min, indicating that convective penetration is modulated by the underlying stable layer.

Figure 10 shows power spectral density contours of convective heat flux fluctuations for the 100% subsolar heating case as a function of angular frequency and height. By considering fluctuations in F_c, we effectively filter out the gravity wave signal since F_c is exactly zero for linear internal gravity waves; that is, w' and θ'' are 90 degrees out of phase for linear gravity waves. Instead, variations in F_c in the penetrative region represent the effect of the stable layer on downflow plumes since most of the convective heat flux is carried by penetrative plumes. As a plume penetrates the underlying stable layer, its motion is modulated with a characteristic timescale N^{-1}, where N is the mean Brunt–Väisälä frequency at the altitude of penetration. In essence, downflow plumes (and thus convective heat flux F_c) experience ''interfacial'' penetrative oscillations with frequencies near the Brunt–Väisälä frequency. These penetrative modes are analogous to surface waves since they occur at the interface between downflow plumes and the underlying stable layer and rapidly evanesce below the penetrative region.

As Fig. 10 shows, such ''interfacial'' oscillations in F_c do occur in the penetrative region (note how the spectral peaks cluster near the dashed curve representing the Brunt–Väisälä frequency). In the convection layer, the spectrum of fluctuations in F_c exhibits significant periods of 30, 46, and 105 min. By contrast, fluctuations in F_c experience peaks with periods of 11, 13, 16, 30,

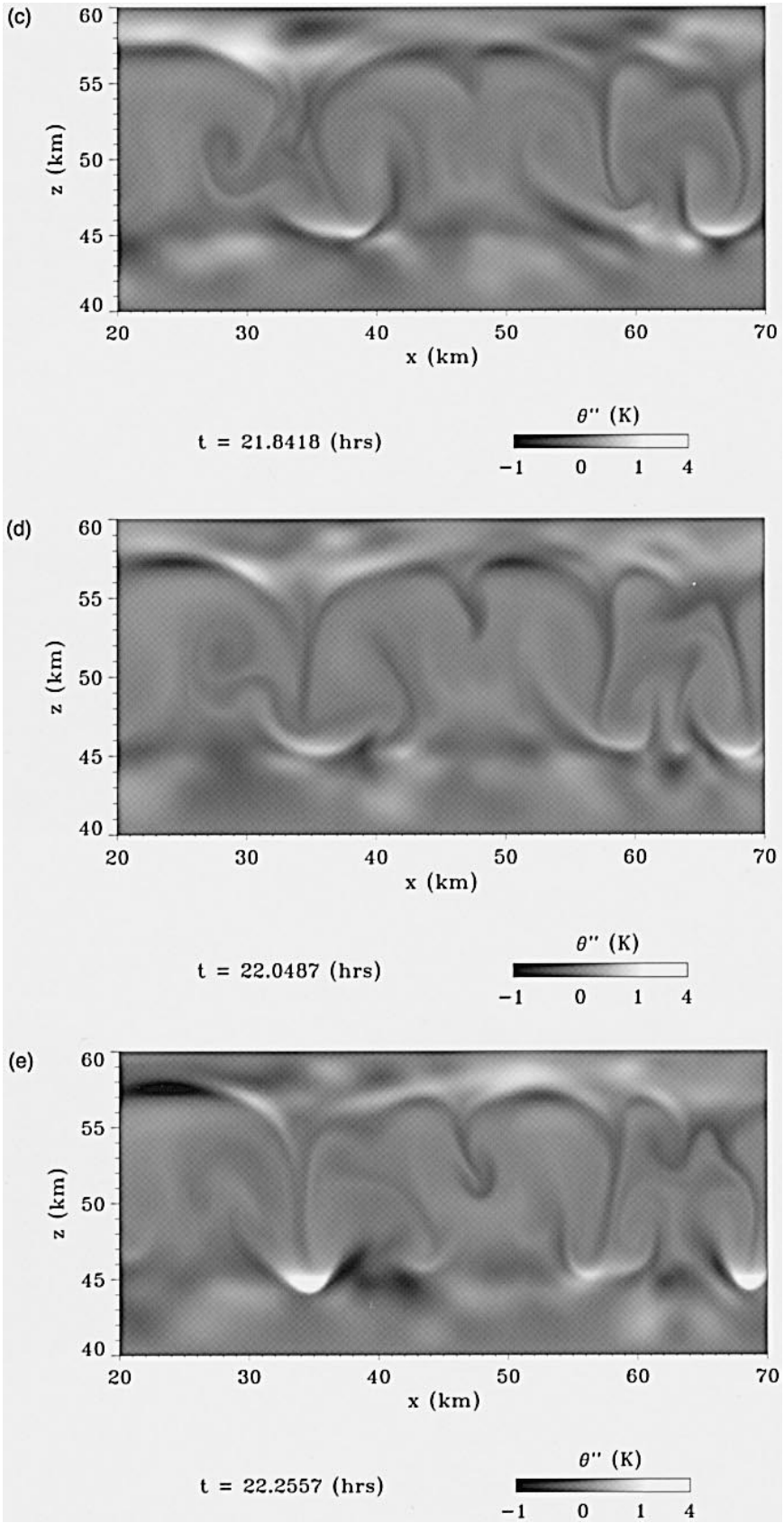

FIG. 8. (*Continued*)

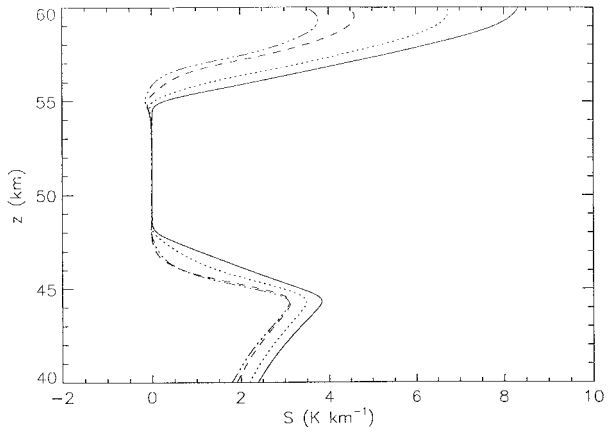

FIG. 9. Altitude profiles of the time-averaged and horizontally averaged static stability for the background state (solid), the 60% subsolar heating case (dot), the 80% subsolar heating case (dash), and the 100% subsolar heating case (dash-triple dot).

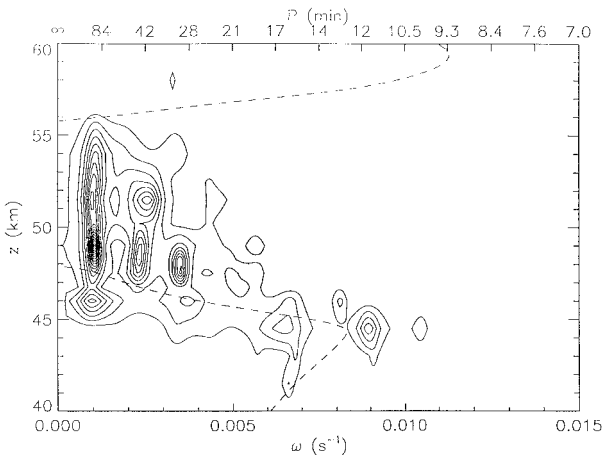

FIG. 10. Power spectral density contours of fluctuations in convective heat flux F_c for the 100% subsolar heating case as a function of angular frequency or period and altitude. The contour interval is 2500 W^2 m^{-4} Hz^{-1}. The maximum power is 4.4×10^4 W^2 m^{-4} Hz^{-1}. The dashed line is the time-averaged and horizontally averaged Brunt–Väisälä frequency.

and 105 min in the penetrative region (~43–47-km altitude). The excited modes in the penetrative region are harmonics of the driving frequencies of convection. The 46-min oscillation ($\omega \sim 2.2 \times 10^{-3}$ s^{-1}) disappears in the underlying stable layer and is replaced by third ($\omega \sim 6.5 \times 10^{-3}$ s^{-1}, or 16-min period) and fourth ($\omega \sim 8.8 \times 10^{-3}$ s^{-1}, or 11-min period) harmonic oscillations. The second harmonic of the 46-min oscillation ($\omega \sim 4.3 \times 10^{-3}$ s^{-1}) is mildly excited in the penetrative region but evanesces deeper in the stable layer. The 13-min mode ($\omega \sim 8.0 \times 10^{-3}$ s^{-1}) excited in the penetrative region is a higher harmonic of the 104-min driving frequency.

The horizontally averaged amount of penetration (~5 km) is significantly larger than Boussinesq parcel methods predict. Consider a parcel of air at the convection layer–stable layer interface. As this parcel travels downward into the stable layer, the parcel velocity decreases until the negative buoyancy of the stable layer halts penetration completely. We can use simple gravity wave theory (Lindzen 1990) to estimate the depth of penetration by this parcel, that is, the maximum displacement of the parcel in a stable environment. The penetration depth is then given by w/N, where w is the parcel velocity at the convection layer–stable layer interface. Parcel velocities of $w \sim 10$ m s^{-1} and Brunt–Väisälä frequencies of $N \sim 5 \times 10^{-3}$ s^{-1} (a characteristic value in the underlying stable layer) give penetration depths of ~2 km. Compressible convection produces penetration depths 2.5 times larger.

d. Gravity waves

Convective penetration and entrainment generate internal gravity waves in the adjacent stable layers (Fig. 8). Gravity waves in the underlying stable layer have characteristic vertical velocities of 1–2 m s^{-1}. Spectral analysis of residual potential temperature at 42-km altitude indicates that these gravity waves have horizontal wavelengths of 5–30 km with a peak horizontal wavelength of 12 km. The waves are ducted horizontally by the overlying convection layer and the lower boundary at 40 km, which causes vertical reflection of waves. Horizontal propagation of waves generated by the penetrating downflow plumes occurs in both directions with a characteristic intrinsic phase speed (as determined from visual tracking of peaks in residual potential temperature) of roughly 10 m s^{-1}, similar to the convective velocities driving the waves. Convective entrainment generates internal gravity waves in the overlying stable layer with vertical velocities of ~0.5–1 m s^{-1}. The waves are ducted horizontally by the convection layer and the upper boundary at 60-km altitude. Spectral analysis of residual potential temperature indicates that internal gravity waves in the upper stable layer have horizontal wavelengths of ~10–25 km at 58-km altitude, and visual tracking of peaks in residual potential temperature reveals intrinsic phase speeds of ~12 m s^{-1}. It should be noted that gravity wave properties in these simulations are strongly influenced by the artificial boundaries at 40 and 60 km altitude and that simulations without these artificial boundaries will possibly produce gravity waves of different wavelengths and phase speeds. More detailed analysis of convectively generated internal gravity waves is required.

Internal gravity waves generated by penetrative convection often interact and modify the convection. The interaction between convection and waves is best seen in a movie of the time history of the deviation potential temperature field. Ducted gravity waves can sway strong penetrative downwellings horizontally by as much as 5 km. For example, the compression region located at horizontal position $x = 37$ km in Fig. 8b has been

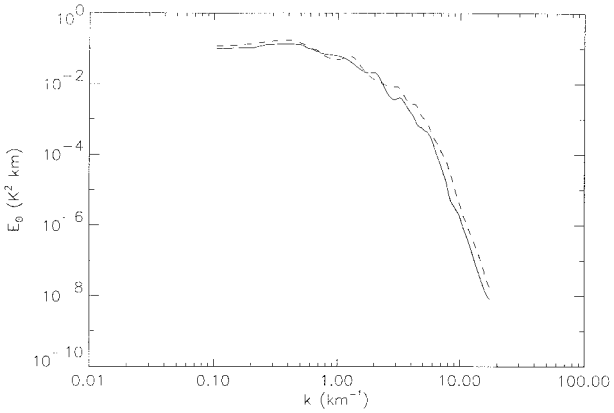

FIG. 11. Power spectral density of potential temperature fluctuations at 52-km altitude as a function of wavenumber. The solid line is for the case with stress-free boundaries and the dashed line is for the case with sponge layer boundaries. The power spectra have been averaged over the last 2.5 hours of simulation time for each run.

pushed horizontally to the right a few kilometers by a passing gravity wave (Fig. 8c). Twelve minutes later, the compression region has swung past its original location and now resides at $x = 35$ km (Fig. 8d). This horizontal motion often diminishes the penetration depth of the downflow plume by decoupling the plume head from the downwelling core and aids in the dissipation of the compressionally heated region. It is important to note, however, that gravity wave feedback on convection in our model will likely be stronger than in the Venus atmosphere because the artificial boundary at 40-km altitude in the model prohibits vertical wave propagation and energy transport out of the computational domain.

To test the effect of wave-reflecting boundaries on convective planform, we performed a calculation with sponge layers at the top and bottom to prevent wave reflection. The results are compared with an impermeable, stress-free boundary simulation with 100% subsolar heating. The horizontal extent for these runs is 60 km. The initial condition for the stress-free case was the final state from $x = 0$ km to $x = 60$ km of the 100% subsolar heating case presented earlier. The same initial condition was used for the sponge layer case except with motionless, unperturbed stable layers to eliminate artificially trapped gravity waves. Both cases were integrated for roughly 13 hours simulation time. Ducted gravity waves in both the underlying and overlying stable regions are present in the stress-free case, while gravity waves in the sponge layer case quickly dampen as they propagate away from the generation region. Figure 11 shows power spectral density of potential temperature fluctuations at 52-km altitude as a function of wavenumber for the two cases. The power spectra are remarkably similar with dominant horizontal scales of roughly 15–30 km, indicating that ducted gravity waves caused by stress-free boundaries have little effect on convective length scales.

4. Discussion

Our simulations of cloud-level compressible convection in the Venus atmosphere are nonlinear, high Rayleigh number calculations that address the style of atmospheric convection on Venus. Many features in our simulations (e.g., extremely narrow downwellings and compressional regions in the underlying stable layer) would not be seen if the Boussinesq or anelastic approximations had been employed. Our fully compressible model provides for deep convection by allowing density stratification over multiple scale heights and includes simulation of local compressional features. Compressibility operates as a positive feedback for generating narrow downwellings by increasing the local density in regions of convergence (Hurlburt et al. 1984). Although internally heated Boussinesq systems are driven by cold, relatively narrow downflow plumes (Peckover and Hutchinson 1973), the feedback mechanism due to compression produces even stronger, more concentrated downwellings. The local compressional regions located at roughly 45-km altitude would not occur in an anelastic or Boussinesq study. Local compressional heating in this region is four orders of magnitude larger than solar heating at that altitude. These compressional regions are an intense local heat source and may account for turbulence observed at 45-km altitude by radio occultation experiments (Woo et al. 1982).

A general characteristic of these simulations is the enhanced vigor of convection with increasing solar heating (increasing Ra_q^*). As solar heating increases, the average kinetic energy of the layer increases, the strength of the downwellings increases, the amount of heat transported by convection rises, penetration extends deeper into the underlying stable layer, and the thickness of the neutrally stable layer increases. The vertical velocities of our simulations, although slightly larger than the *Vega* balloon velocities, are consistent with the *Vega* balloon measurements since the balloons sampled in the early morning. Any future probes or balloons into the subsolar region should expect to find a thicker neutrally stable layer with more vigorous convection than previously measured. Also, the *Vega* balloons drifted in the relatively quiescent upper part of the cloud-level convective layer. Convection is much more vigorous near the bottom of the layer where intense downwellings enter the underlying stable layer. Any future balloons placed in the cloud-level convective layer will have to be designed to withstand more vigorous motions if the more active part of the convection layer is to be probed.

The value of eddy diffusion for these calculations is 155 $\mathrm{m^2\ s^{-1}}$. At present, this value should be considered an upper bound for eddy diffusion in the Venus atmosphere. Estimates from photochemical modeling suggest that the diffusion coefficient is two orders of magnitude smaller at $\sim$2 $\mathrm{m^2\ s^{-1}}$ (Krasnopolsky and Parshev 1981, 1983; Krasnopolsky 1985; Yung and DeMore 1982).

This value of eddy diffusion may not be appropriate for modeling small-scale turbulence since eddy diffusion in photochemical models also parameterizes large-scale dynamics. However, if a lower value of eddy diffusion were valid at cloud levels, the Rayleigh number would increase and more intense, turbulent convection would occur in the cloud region. Penetration should be significantly deeper and mixing much stronger for extremely high Rayleigh number convection.

The complex dynamics of the lower penetrative region has significant implications for the microphysical structure of the lower cloud region. The lower Venus cloud from 47.5 to 50.5 km consists of sulfuric acid droplets and crystals with optical depths from 6 to 12 (Knollenberg and Hunten 1980). Vigorous mixing of the lower cloud should occur due to strong penetrative convection in the region. The cold narrow downwellings and the mechanically squeezed plume air could induce condensation of sulfuric acid while the compressionally heated region could result in significant evaporation of the clouds. Thus, the nonlinear dynamics of the penetrative region could result in rapid variation of optical depth in the lower cloud. Furthermore, internal gravity waves in the underlying stable layer generated by penetrative convection could cause temporal and spatial heterogeneities in the lower cloud haze below the cloud deck. These variations would have characteristic length scales of 5–30 km in the penetrative region.

The agreement between mixing length theory and the *Vega* balloon measurements is fortuitous. Mixing length theory matches the *Vega* balloon measurements because the measurements were taken at the top of the layer where convection originates and the velocities are smaller (Fig. 5). If the measurements had been taken deeper in the convection layer, higher velocities would have been observed. Mixing length treatments are intended to represent the average state of the convection layer, yet our simulations of cloud-level convection on Venus indicate otherwise. Typical velocities for the 100% subsolar case are 10 m s^{-1}, or roughly three times larger than mixing length estimates. Similarly, parcel methods underestimate the depth of convective penetration by a factor of 2.5. These discrepancies are due to compressibility effects that are not adequately treated in Boussinesq models. Kinetic energy in the convection layer is not balanced by buoyancy work as assumed by mixing length theory, but instead is balanced by buoyancy, pressure, and viscous work.

Studies that utilize mixing length theory to parameterize convection in the Venus atmosphere underestimate dynamical processes due to convection. For example, Leroy and Ingersoll (1995, 1996) use mixing length theory to associate the convective heat flux with vertical velocities in the cloud-level convection layer. These velocities ($\sim$3 m s^{-1}), in turn, generate internal gravity waves in the overlying stable layer with phase speeds comparable to the convective velocities. Our simulations also exhibit gravity wave phase speeds comparable to average convective velocities, but our velocities are three to four times larger. Gravity waves with phase speeds on the order of 10 m s^{-1} would propagate to higher altitudes before being absorbed by critical layers and may contribute to the Venus superrotation more strongly than the low phase speed waves of Leroy and Ingersoll (1995).

The transfer of convective energy to higher frequencies in the underlying stable layer is a striking result of our simulations. By inducing oscillations at the plume–stable layer interface, the underlying stable layer modulates the depth of penetration and the amount of heat transferred downward by penetrative plumes. The dominant interfacial fluctuations in convective heat flux in the penetrative region are near the Brunt–Väisälä frequency and are higher harmonics of the convective driving modes. Internal gravity waves are also generated by convective downdrafts in the penetrative region. While the present study can qualitatively describe these waves, reflections from the lower boundary at 40-km altitude preclude a detailed quantitative study of the properties of the waves. Further investigations with a lower boundary below 30-km altitude will be necessary to determine which gravity wave modes are excited by cloud-level convection and which modes can propagate deep into the atmosphere of Venus.

The horizontal scale of convection cells in our simulations is 15–30 km, an order of magnitude smaller than observed in the UV images of the cloud tops. A physical mechanism absent in our model must account for the large horizontal cell sizes on Venus if the observed cellular structure is due to convection. Anisotropic eddy diffusion preferentially spreads material horizontally and may elongate convection cells in the cloud region. The amount of anisotropy required to give aspect ratios of 100 (Covey and Schubert 1981) is consistent with the degree of anisotropy observed in Earth's atmosphere (Pedlosky 1987). The penetrative convection hypothesis of Baker and Schubert (1992) requires significant nonlinear interaction between cloud-level convection, lower atmosphere convection, and gravity waves in the stable layer between. To test this hypothesis, we must extend the lower boundary of our model from 40-km altitude to below 18-km altitude to include both convection regions in the simulation. Yet another possibility to explain the large cell sizes in the observations is horizontally varying absorption of solar radiation due to heterogeneous concentrations of absorbers. Toigo et al. (1994) show that differential horizontal absorption of sunlight may support large mesoscale cells in a thin layer at the cloud tops. However, as Toigo and coworkers state, the ''arguments made in this paper do not address the fundamental origin of the mesoscale cells.'' The cause of the large cellular features observed near the subsolar point remains uncertain and warrants further investigation.

Acknowledgments. The calculations were performed

on the National Center for Supercomputing Applications (NCSA) CM-5 and the NASA Ames Research Center NAS CM-5. This work was supported by NASA Planetary Atmospheres Program under Grant NAGW-1874. We also appreciate the thoughtful reviews by two anonymous referees.

REFERENCES

Agee, E. M., 1987: Mesoscale cellular convection over the oceans. *Dyn. Atmos. Ocean,* **10,** 317–341.

Asselin, R., 1972: Frequency filter for time integrations. *Mon. Wea. Rev.,* **100,** 487–490.

Baker, R. D., II, and G. Schubert, 1992: Cellular convection in the atmosphere of Venus. *Nature,* **355,** 710–712.

Belton, M. J. S., G. R. Smith, G. Schubert, and A. D. Del Genio, 1976: Cloud patterns, waves and convection in the Venus atmosphere. *J. Atmos. Sci.,* **33,** 1394–1417.

——, P. J. Gierasch, M. D. Smith, P. Helfenstein, P. J. Schinder, J. B. Pollack, K. A. Rages, A. P. Ingersoll, K. P. Klassen, J. Veverka, C. D. Anger, M. H. Carr, C. R. Chapman, M. E. Davies, F. P. Fanale, R. Greeley, R. Greenberg, J. W. Head III, D. Morrison, G. Neukum and C. B. Pilcher. 1991: Images of the Venus cloud deck from Galileo. *Science,* **253,** 1531–1536.

Blamont, J. E., R. E. Young, A. Seiff, B. Ragent, R. Sagdeev, V. M. Linkin, V. V. Kerzhanovich, A. P. Ingersoll, D. Crisp, L. S. Elson, R. A. Preston, G. S. Golitsyn and V. N. Ivanov, 1986: Implications of the VEGA balloon results for Venus atmospheric dynamics. *Science,* **231,** 1422–1425.

Brandes, E. A., 1978: Mesocyclone evolution and tornadogenesis: Some observations. *Mon. Wea. Rev.,* **106,** 995–1011.

Covey, C. C., and G. Schubert, 1981: Mesoscale cellular convection in the clouds of Venus. *Nature,* **290,** 17–20.

Cox, J. P., and R. T. Giuli, 1968: *Principles of Stellar Structure*: Vol. 1. *Physical Principles.* Gordon and Breach, 568 pp.

Emanuel, K. A., 1994: *Atmospheric Convection.* Oxford University Press, 580 pp.

Graham, E., 1975: Numerical simulation of two-dimensional compressible convection. *J. Fluid Mech.,* **70,** 689–703.

Hansen, C. J., and S. D. Kawaler, 1994: *Stellar Interiors: Physical Principles, Structure, and Evolution.* Springer-Verlag, 445 pp.

Hinson, D. P., and J. M. Jenkins, 1995: Magellan radio occultation measurements of atmospheric waves on Venus. *Icarus,* **114,** 310–327.

Holton, J. R., 1979: *An Introduction of Dynamic Meteorology.* 2d ed. Academic Press, 391 pp.

Hou, A. Y., and R. M. Goody, 1989: Further studies of the circulation of the Venus atmosphere. *J. Atmos. Sci.,* **46,** 991–1001.

Howard, H. T., G. L. Tyler, G. Fjeldbo, A. J. Kilore, G. S. Levy, D. L. Brunn, R. Dickenson, R. E. Edelson, W. L. Martin, R. B. Postal, B. Seidel T. T. Sesplaukis, D. L. Shirley, C. T. Stelzried, D. N. Sweetnam, A. I. Zygielbaum, P. B. Esposito, J. D. Anderson, I. I. Shapiro and R. D. Reasenberg. 1974: Venus: Mass, gravity field, atmosphere, and ionosphere as measured by the Mariner 10 dual frequency radio system. *Science,* **183,** 1297–1301.

Hurlburt, N. E., J. Toomre, and J. M. Massaguer, 1984: Two-dimensional compressible convection extending over multiple scale heights. *Astrophys. J.,* **282,** 557–573.

——, ——, and ——, 1986: Nonlinear compressible convection penetrating into stable layers and producing internal gravity waves. *Astrophys. J.,* **311,** 563–577.

Ingersoll, A. P., D. Crisp, A. W. Grossman, and the VEGA Balloon Science Team, 1987: Estimates of convective heat fluxes and gravity wave amplitudes in the Venus middle cloud layer from VEGA Balloon measurements. *Adv. Space. Res.,* **7,** (12)343–(12)349.

Jenkins, J. M., P. G. Steffes, D. P. Hinson, J. D. Twicken, and G. L. Tyler, 1994: Radio occultation studies of the Venus atmosphere with the Magellan spacecraft. 2. Results from the October 1991 experiments. *Icarus,* **110,** 79–94.

Jones, P. W., 1991: Compressible convection and pulsations on parallel computers. Ph.D. thesis, University of Colorado at Boulder, 196 pp. [Available from University of Colorado, Boulder, CO 80309.]

Knollenburg, R. G., and D. M. Hunten, 1980: The microphysics of the clouds of Venus: Results of the Pioneer Venus particle size spectrometer experiment. *J. Geophys. Res.,* **85,** 8039–8058.

Krasnopolsky, V. A., 1985: Chemical composition of Venus clouds. *Planet. Space Sci.,* **33,** 109–117.

——, and V. A. Parshev, 1981: Chemical composition of the atmosphere of Venus. *Nature,* **292,** 610–613.

——, and ——, 1983: Photochemistry of the Venus atmosphere. *Venus,* D. M. Hunten, L. Colin, T. M. Donahue, and V. I. Moroz, Eds., The University of Arizona Press, 431–458.

Leroy, S. S., 1994: Convectively generated internal gravity waves in Venus's middle atmosphere: Momentum transport and radio scintillations. Ph.D. thesis, California Institute of Technology, 204 pp. [Available from California Institute of Technology, Pasadena, CA 91125.]

——, and A. P. Ingersoll, 1995: Convective generation of gravity waves in Venus's atmosphere: Gravity wave spectrum and momentum transport. *J. Atmos. Sci.,* **52,** 3717–3737.

——, and ——, 1996: Radio scintillations in Venus's atmosphere: Application of a theory of gravity wave generation. *J. Atmos. Sci.,* **53,** 1018–1028.

Lindzen, R. S., 1990: *Dynamics in Atmospheric Physics.* Cambridge University Press, 310 pp.

Linkin, V. M., V. V. Kerzhanovich, A. N. Lipatov, K. M. Pichkadze, A. A. Shurupov, A. V. Terterashvilli, A. P. Ingersoll, D. Crisp, A. W. Grossman, R. E. Young, A. Seiff, B. Ragent, J. E. Blamont, L. S. Elson, and R. A. Preston. 1986: VEGA balloon dynamics and vertical winds in the Venus middle cloud region. *Science,* **231,** 1417–1419.

Moore, D. R., and N. O. Weiss, 1973: Two-dimensional Rayleigh–Benard convection. *J. Fluid Mech.,* **58,** 289–312.

Murray, B. C., M. J. S. Belton, G. E. Danielson, M. E. Davies, D. Gault, B. Hapke, B. O'Leary, R. G. Strom, V. Suomi, and N. Trask. 1974: Venus: Atmospheric motion and structure from Mariner 10 pictures. *Science,* **183,** 1307–1315.

Peckover, R. S., and I. H. Hutchinson, 1974: Convective rolls driven by internal heat sources. *Phys. Fluids,* **17,** 1369–1371.

Pedlosky, J., 1987: *Geophysical Fluid Dynamics.* Springer-Verlag, 710 pp.

Pollack, J. B., and R. Young, 1975: Calculations of the radiative and dynamical state of the Venus atmosphere. *J. Atmos. Sci.,* **32,** 1025–1037.

——, O. B. Toon, and R. Boese, 1980: Greenhouse models of Venus' high surface temperature, as constrained by Pioneer Venus measurements. *J. Geophys. Res.,* **85,** 8223–8231.

Rossow, W. B., A. D. Del Genio, S. S. Limaye, L. D. Travis, and P. H. Stone, 1980: Cloud morphology and motions from Pioneer Venus images. *J. Geophys. Res.,* **85,** 8107–8128.

Schinder, P. J., P. J. Gierasch, S. S. Leroy, and M. D. Smith, 1990: Waves, advection, and cloud patterns on Venus. *J. Atmos. Sci.,* **47,** 2037–2052.

Schubert, G., 1983: General circulation and the dynamical state of the Venus atmosphere. *Venus,* D. M. Hunten, L. Colin, T. M. Donahue, and V. I. Moroz, Eds., The University of Arizona Press, 681–765.

——, and R. L. Walterscheid, 1984: Propagation of small-scale acoustic-gravity waves in the Venus atmosphere. *J. Atmos. Sci.,* **41,** 1202–1213.

Seiff, A., D. B. Kirk, R. E. Young, R. C. Blanchard, J. T. Findlay, G. M. Kelly, and S. C. Sommer, 1980: Measurements of thermal structure and thermal contrasts in the atmosphere of Venus and related dynamical observations: Results from the four Pioneer Venus probes. *J. Geophys. Res.,* **85,** 7903–7933.

——, R. E. Young, R. Haberle, and H. Houben, 1992: The evidences of waves in the atmospheres of Venus and Mars. *Venus and Mars: Atmospheres, Ionospheres, and Solar Wind Interactions, Geophys. Monogr.* No. 66, Amer. Geophys. Union, 73–89.

Sparrow, E. M., R. J. Goldstein, and V. K. Jonsson, 1964: Thermal instability in a horizontal fluid layer: Effect of boundary conditions and non-linear temperature profile. *J. Fluid Mech.,* **18,** 513–528.

Spiegel, E. A., and G. Veronis, 1960: On the Boussinesq approximation for a compressible fluid. *Astrophys. J.,* **131,** 442–447.

Staley, D. O., 1970: The adiabatic lapse rate in the Venus atmosphere. *J. Atmos. Sci.,* **27,** 219–223.

Thirby, R., 1970: Convection in an internally-heated fluid. *J. Fluid Mech.,* **44,** 673–693.

Toigo, A., P. J. Gierasch, and M. D. Smith, 1994: High resolution cloud feature tracking on Venus by Galileo. *Icarus,* **109,** 318–336.

Tomasko, M. G., 1983: The thermal balance of the lower atmosphere of Venus. *Venus,* D. M. Hunten, L. Colin, T. M. Donahue, and V. I. Moroz, Eds., The University of Arizona Press, 604–641.

——, P. H. Smith, V. E. Suomi, L. A. Sromovsky, H. E. Revercomb, F. W. Taylor, D. J. Martonchik, A. Seiff, R. Boese, J. B. Pollack, A. P. Ingersoll, G. Schubert and C. C. Covey. 1980: The thermal balance of Venus in light of the Pioneer Venus mission. *J. Geophys. Res.,* **85,** 8187–8199.

——, L. R. Doose, and P. H. Smith, 1985: The absorption of solar energy and the heating rate in the atmosphere of Venus. *Adv. Space Res.,* **5,** 71–79.

Tritton, D. J., 1975: Internally heated convection in the atmosphere of Venus and in the laboratory. *Nature,* **257,** 110–112.

Woo, R., J. W. Armstrong, and A. J. Kliore, 1982: Small-scale turbulence in the atmosphere of Venus. *Icarus,* **52,** 335–345.

Young, R. E., R. L. Walterscheid, G. Schubert, A. Seiff, V. M. Linkin, and A. N. Lipatov, 1987: Characteristics of gravity waves generated by surface topography on Venus: Comparison with the VEGA balloon results. *J. Atmos. Sci.,* **44,** 2628–2639.

Yung, Y. L., and W. B. DeMore, 1982: Photochemistry of the stratosphere of Venus: Implications for atmospheric evolution. *Icarus,* **51,** 199–247.